ROYAL SOCIETY
OF CHEMISTRY

PAPER

Check for updates

Optimisation of the mechanochemical synthesis time of thermoelectric material Mg_3Sb_2–Mg_3Bi_2

Alena Mikhailova, [*ab] Aleksandr Markin, [a] Kseniia Shcherbakova, [*ab] Yurii Kuznetsov, [c] Vlad Dybov [a] and Natalia Tabachkova [b]

The present paper sets out the optimisation of the mechanochemical synthesis process of the thermoelectric material $Mg_{3.2}Sb_{1.5}Bi_{0.45}Te_{0.05}$. The current study investigates the effect of varying the time in the range from 1 to 9 hours on the phase composition, morphology of powders and thermoelectric properties of the samples obtained. It was established that the formation of the α-phase is complete after a period of 5 hours of mechanochemical synthesis. It was determined through the utilisation of scanning electron microscopy, in conjunction with an image analysis algorithm written in Python, that by 5 hours, a median particle size of 3.7 μm and the most uniform size distribution are achieved. It has been demonstrated that an increase in the duration to 7–9 hours results in particle agglomeration without any alteration to the phase composition. It was established that the specimen extracted from the powder following a period of 5 hours of mechanochemical synthesis possesses a thermoelectric figure of merit of $zT \approx 0.92$ at 765 K. This investigation enabled the determination of the optimal time for the mechanochemical synthesis of the thermoelectric material $Mg_{3.2}Sb_{1.5}Bi_{0.45}Te_{0.05}$ through the utilisation of computer vision methodologies.

1 Introduction

The development of thermoelectric (TE) materials for utilisation in thermoelectric generators (TEGs) represents significant scientific and practical interest, owing to their capacity to directly convert thermal energy into electricity. TEGs offer distinct advantages, including autonomous operation, the absence of moving parts, and the mitigation of vibrations. Consequently, TEGs have emerged as a promising solution for the creation of autonomous sources of electricity and for integration into energy systems with the aim of enhancing overall efficiency.[1]

TEGs are composed of n- and p-type legs of TE materials.[1,2] The efficiency of these TEGs is determined by a dimensionless parameter known as the TE figure of merit:[3] $zT = (\alpha^2\sigma/\kappa)T$, where σ is the electrical conductivity ($ohm^{-1} cm^{-1}$), α is the Seebeck coefficient ($\mu V K^{-1}$), $\kappa = \kappa_{lat} + \kappa_{el}$ is the total thermal conductivity ($W (m^{-1} K^{-1})$), with κ_{lat} and κ_{el} representing the lattice and electronic components, respectively, and T is the absolute temperature (K).

In recent years, there has been a particular focus on materials with low-symmetry crystal structures, such as Zintl phases,

which are characterised by low lattice thermal conductivity.[4] One of the most well-known representatives of this group is a compound based on Mg_3Sb_2 (space group $P\bar{3}m1$), which is considered to be the most promising for TE applications in the medium temperature range. The solid solution $Mg_3(Sb,Bi)_2$ has been shown to exhibit a record zT value of 2.04 at 798 K.[5] This material is considered an environmentally friendly alternative to traditional lead tellurides for n-legs, while possessing comparable TE characteristics.[6–8]

The hexagonal structure of Mg_3Sb_2 and Mg_3Bi_2 is identical and contributes to the formation of a continuous series of solid solutions.[9,10] In the resulting solid solution, the average effective electron mass decreases, thereby increasing the mobility and, accordingly, the electrical conductivity of this compound.[11] Furthermore, the lattice thermal conductivity will also decrease due to the Bi impurity, which is the centre of impurity scattering.[12] Considering the properties of Mg_3Bi_2 and Mg_3Sb_2, it can be concluded that the width of the $Mg_3Sb_{2-x}Bi_x$ band gap will decrease with increasing Bi content.[8,11,13]

In order to regulate the type of conductivity and optimise the charge carrier concentration, Sb is substituted with elements from group 16, such as Te.[8] The mechanism of action underpinning this phenomenon involves the replacement of the Sb^{3-} anion with Te^{2-}, a process which results in the generation of an additional free electron for each impurity atom. This, in turn, ensures stable n-type conductivity.[8] This doping is critical for compensating for natural defects—magnesium vacancies, which in an undoped state create p-type conductivity.[14–16]

a State Research and Design Institute of Rare Metal Industry (JSC "Giredmet"), Elektrodnaya St. 2, Build. 1, Moscow, Russia. E-mail: m155333@edu.misis.ru

b National University of Science and Technology MISIS, Leninsky Av. 4, Moscow, Russia

c Lobachevsky State University of Nizhny Novgorod, Gagarin Av. 23, Build. 2, Nizhny Novgorod, Russia

Moreover, it is imperative to acknowledge the pivotal influence of the synthesis method and sintering conditions on the TE properties of Mg_3Sb_2.[10,17–29] Presently, the predominant method for producing this material is mechanochemical synthesis (MCS), which spans a duration of 10 to 48 hours.[6,17,19,20,25,29,30] However, in the majority of studies, MCS conditions, including grinding duration, are selected empirically. The optimisation of the MCS time has been demonstrated to engender a substantial reduction in energy costs, whilst concomitantly effecting the scale-up of the production of n-type TEMs.

The morphological characteristics of powders play a pivotal role in the development of TE materials. It is imperative to undertake a comprehensive investigation into the impact of MCS time on the phase composition and particle size distribution of powders. Determining the particle size distribution of powders obtained in the MCS process is a laborious task when using standard methods such as laser diffraction and dynamic light scattering. The measurement of the particle size distribution of this powder is complicated by the presence of a wide range of particle sizes, which necessitates the implementation of a combination of methods to achieve an accurate measurement. It is imperative to note that both methods demand meticulous sample preparation in accordance with the stipulated methodological regulations. This renders the task arduous and protracted, and the most minuscule deviation from the methodological guidelines can result in erroneous measurements. Therefore, to minimise uncertainties and errors in particle size measurements and reduce labor intensity, it is proposed to apply a modern approach to powder morphology analysis, combining scanning electron microscopy (SEM) with an image analysis algorithm. This method facilitates more precise determination of the particle size distribution of powders comprising a wide range of particle sizes.

The objective of this study is to optimise the time required to obtain $Mg_{3.2}Sb_{1.5}Bi_{0.45}Te_{0.05}$ using the MCS method, apply digital methods of image analysis of particle size distribution, and study the thermoelectric characteristics of the obtained samples.

2 Experimental

2.1 Materials synthesis

Samples of stoichiometric composition $Mg_{3.2}Sb_{1.5}Bi_{0.45}Te_{0.05}$ were obtained by MCS with varying times from 1 to 9 hours. The following components were used as starting materials: Mg (powder, 99.5%), Sb (granules, 99.999%), Bi (granules, 99.999%), and Te (granules, 99.999%). The initial components in stoichiometric proportions were ground in an agate mortar to a micro-powder state, which was then transferred into a 250 ml stainless steel milling chamber. The powder was loaded and unloaded in a glove box under an argon atmosphere. 30 ml of surfactant–hexane was added to the mixture to inhibit agglomeration during milling. The synthesis was carried out in a planetary ball mill (Retsch PM 400 MA). The ball-to-powder (BPR) weight ratio ranged from 5 : 1 to 10 : 1 ($d = 5$ mm, stainless steel). The total number of balls was 700–1000 pcs. The

rotational speed of the milling chamber was maintained within the range of 300 to 500 rpm. Following the grinding process, the hexane was evaporated at ambient temperature. Subsequently, the powder was subjected to a sieving process, employing a sieve with a mesh size of 250 μm. The resulting powder was consolidated using the spark plasma sintering (SPS) method on an SPS-511S (Dr Sinter Lab., Japan) at 650 °C and 5 min under 50 MPa. The obtained samples were subjected to a process of annealing for the elimination of residual stresses in crucibles at temperatures ranging from 400 to 600 °C in an argon atmosphere.

2.2 Research methods

The phase analysis was performed by X-ray diffraction (XRD) using a Bruker D2 Phaser diffractometer ($Cu_{K\alpha}$ radiation, $\lambda = 1.5418$ Å). Phase identification was performed using the ICDD PDF-4+ database. The morphology of the powders was studied by SEM using an FEI Quanta FEG 250 microscope. All powders were imaged at an accelerating voltage of 10 kV in secondary electron mode.

The particle size distribution of the powders was analysed using SEM. The powders were dispersed in a specialised apparatus and placed on the surface of double-sided carbon tape under a powerful air flow. It is evident that the repeated high-energy collisions of powder particles with the walls of the device resulted in effective dispersion and the subsequent monolayer placement of the powder on the stage. Subsequently, a set of images (8–10 pieces) was processed using an algorithm written in the Python programming language. The implementation of this algorithm was facilitated by the utilisation of open-source libraries: Numpy, scikit-image, Pandas, Matplotlib, and Seaborn. The primary stages of image processing and analysis comprised the following: sequential automatic image loading, noise filtering, brightness thresholding employing Otsu's method,[31] powder particle segmentation, calculation of particle geometric dimensions, and visualisation of the analysis results.

Electrical resistance was measured using a four-probe method, while the Seebeck coefficient was measured in parallel using a differential method. The measurements were conducted within a helium atmosphere using a ZEM-3 setup (ULVAC Riko, Japan). Thermal conductivity was measured using the steady-state heat flow method. The density of the samples was measured using the hydrostatic weighing method. Given that the relative density of the samples was 87–94%, porosity correction according to the Maxwell–Eucken equation was applied during the processing of the experimental data (σ and κ).[32] The errors in measuring the Seebeck coefficient, electrical conductivity, and total thermal conductivity were approximately 5%. All measurements were conducted within the temperature range of 390–770 K.

3 Results and discussion

The diffractograms of powders obtained by MCS with varying times from 1 to 9 hours are shown in (Fig. 1). A thorough
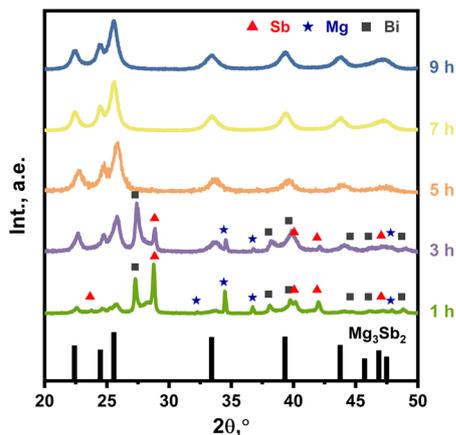
Fig. 1 Powder XRD patterns of the samples of stoichiometric composition $Mg_{3.2}Sb_{1.5}Bi_{0.45}Te_{0.05}$ were obtained by MCS with varying times from 1 to 9 hours. Bragg's reflections for the Mg_3Sb_2 phase are indicated by black ticks on the bottom part of the figure.

analysis of the diffraction patterns revealed that in the samples after 1 and 3 hours, the initial elements (Mg and Sb) and intermediate phases predominate. However, after 1 hour, the formation of the target α-phase has already commenced. Following a grinding process that lasted for a period of 5 hours, the α-phase was the only phase detected. An extension of the grinding time to 9 hours did not result in any discernible alterations to the phase composition, suggesting that phase-forming processes are complete by 5 hours. Analysis of the phase composition of the powders indicates the potential for the acquisition of the material exhibiting the requisite α-phase after 5 hours of grinding.

The morphology of powders obtained by MCS with varying times from 1 to 9 hours is illustrated in (Fig. 2). A thorough analysis of the morphological characteristics indicated a discernible alteration in the powder parameters, contingent on the duration of the processing procedure. Furthermore, the process of phase formation in a compound can be described by morphological characteristics. Following a period of grinding that lasted for 1 hour, a substantial variation in the particle size was observed, with both large and small fractions being present. Furthermore, the presence of numerous unreacted precursors becomes evident, as evidenced by the presence of different phases in the powder diffractogram. Subsequent to a duration of 3 hours, no significant alterations in the dimensions of the
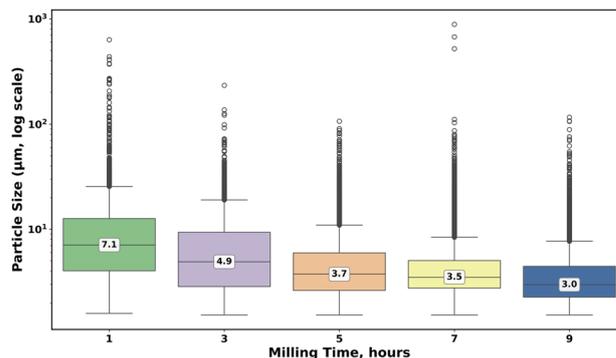

Fig. 3 boxplot of the distribution of the linear dimensions of the particles and the median values of powders of stoichiometric composition $Mg_{3.2}Sb_{1.5}Bi_{0.45}Te_{0.05}$ obtained by MCS with varying times from 1 to 9 hours.

particles were detected. However, evidence of mechanical activation became apparent, as indicated by the partial destruction of large particles and the subsequent formation of smaller fragments. Furthermore, there are precursors that have not reacted. However, the diffractogram presented in (Fig. 1) indicates a quantitative increase in the main phase Mg_3Sb_2. The most significant alterations in morphology were documented following a grinding duration of 5 hours. The powders exhibited the formation of finely dispersed granules, distinguished by their irregular morphology. This assertion is substantiated by the observation that, subsequent to a grinding period of 5 hours, the diffractogram of the samples exhibits exclusively the presence of the requisite phase. As the duration of the process is increased to a period of 7 hours, the process of particle aggregation with the formation of large, loose agglomerates becomes evident. Following a 9-hour grinding process, a slight decrease in the size of the agglomerates was observed. The data obtained suggest that the morphological changes undergone during the MSC process are of a complex nature, encompassing the dispersion stage (1–5 hours) and subsequent aggregation stage (7–9 hours) of particles.

The evaluation of the particle size distribution was conducted through the analysis of SEM images of powders obtained at varying MCS times, employing the technique of particle digitisation. The results of the analysis are presented in (Fig. 3) in the form of a boxplot, showing the dependence of linear particle sizes and median values on grinding time. Following a period of 1 hour during which grinding was undertaken, the median
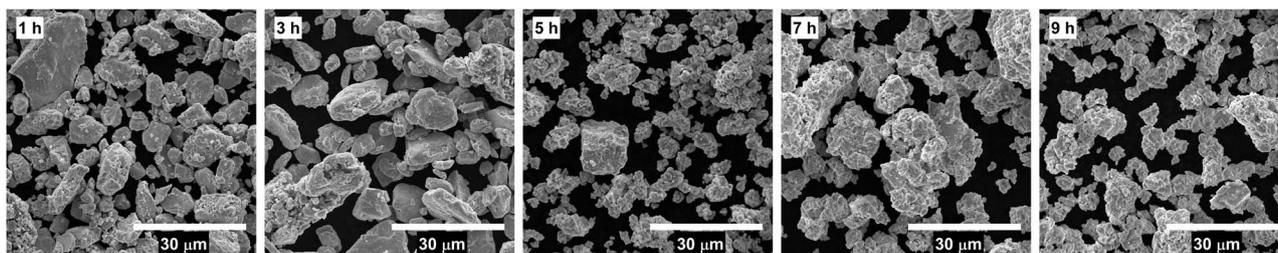

Fig. 2 SEM micrographs of powders of stoichiometric composition $Mg_{3.2}Sb_{1.5}Bi_{0.45}Te_{0.05}$ obtained by MCS with varying times from 1 to 9 hours.

particle size was determined to be 7.1 μm, with a significant spread of values. As demonstrated in Fig. 3, the median size decreased to 4.9 μm after 3 hours of milling. The most significant milling was observed after 5 hours of grinding with a median size of 3.7 μm. It is worthy of note that, at an MCS time of 7–9 hours, the particle size stabilised at approximately 3 μm. This finding suggests that the grinding limit had been reached under these specific MCS conditions. The results obtained are consistent with those of the SEM data. In particular, it was found that after 5 hours of MCS, the average particle size reached 3.7 μm. The results obtained demonstrate that 100% of the powder particles after 5 and 9 hours of grinding are in the range up to 100 μm. However after 1 and 7 hours 100% of the

Fig. 4 Powder XRD patterns of the samples of stoichiometric composition $Mg_{3.2}Sb_{1.5}Bi_{0.45}Te_{0.05}$ obtained by MCS with varying times from 1 to 9 hours and after SPS. Bragg's reflections for the Mg_3Sb_2 phase are indicated by black ticks on the bottom part of the figure.

particles are in the range up to 1000 μm. This discrepancy is presumably attributable to the presence of the unmilled material for a duration of 1 hour, and to the accumulation of agglomerates over a period of 7 hours.

Fig. 4 presents the diffractograms of the sintered samples of $Mg_{3.2}Sb_{1.5}Bi_{0.45}Te_{0.05}$ with varying MCS times of the initial powder. Analysis of the diffraction patterns revealed that the α-phase was the sole phase detected in all of the samples analysed.

Fig. 5 presents the SEM images of the fracture. The sample obtained after 1 hour of MCS was characterised by a loose, heterogeneous structure with pronounced residual porosity, indicating insufficient powder grinding for effective compaction. The extension of the grinding time to 3 hours resulted in the formation of a virtually pore-free, dense structure, characterised by the presence of large, well-defined grains exhibiting a characteristic lamellar morphology. This phenomenon can be attributed to the crystallography of the compound. Subsequent MCS in the samples after 5 and 7 hours resulted in further grinding of the structural elements. As demonstrated in the sample after 7 hours, the lamellar structure is observed to practically disappear, transforming into a fine-grained or submicron structure. This finding indicates that the peak structural dispersion has been achieved. However, following a period of 9 hours of MCS, an unanticipated coarsening of the structure and a reappearance of lamellarity are observed. This phenomenon can be interpreted as the result of abnormally rapid grain growth and recrystallisation during sintering, caused by excessive accumulation of defects and energy in the powder due to excessively protracted grinding. Consequently, the optimal MCS time ensuring maximum structure refinement is presumably in the range of 5–7 hours.
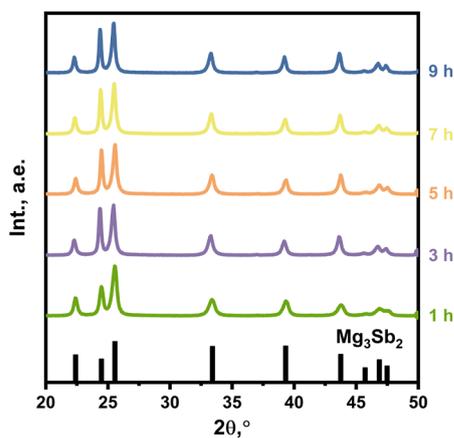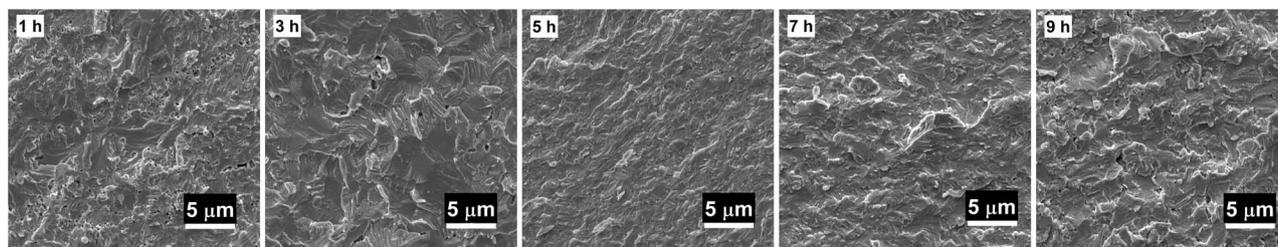

Fig. 5 The SEM micrograph of the fracture surface of bulk $Mg_{3.2}Sb_{1.5}Bi_{0.45}Te_{0.05}$ samples obtained by MCS with varying times from 1 to 9 hours and after SPS.

Table 1 Densities of bulk $Mg_{3.2}Sb_{1.5}Bi_{0.45}Te_{0.05}$ samples obtained with increasing MCS milling time and after SPS

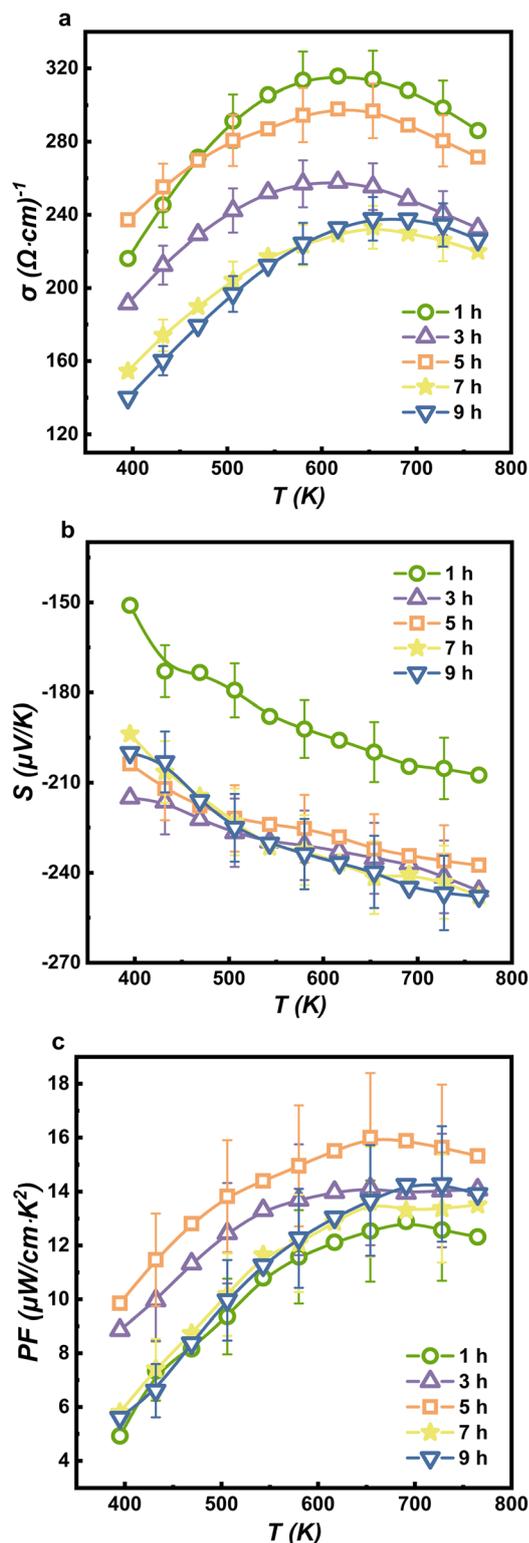| MCS time, hours	Sintering		Annealing	
	Density, g cm^{-3}	Relative density, %	Density, g cm^{-3}	Relative density, %
1	4.0772	87.7	4.0725	87.6
3	4.3582	93.8	4.3580	93.8
5	4.3385	93.3	4.3302	93.2
7	4.3567	93.7	4.3491	93.6
9	4.3163	92.9	4.3098	92.7

Fig. 6 Temperature dependencies of (a) electrical conductivity, (b) Seebeck coefficient, and (c) power factor of bulk $Mg_{3.2}Sb_{1.5}Bi_{0.45}Te_{0.05}$ samples obtained by MCS with varying times from 1 to 9 hours and after SPS.

The aforementioned trend is also replicated in the measured densities of sintered and annealed samples, as presented in Table 1. Following the completion of the sintering process after

1 hour of MCS, the resultant sample exhibited the lowest density, while the remaining samples demonstrated an approximate density of 93%. Following the process of annealing, a decline in the density was observed for all samples. This phenomenon is likely attributable to microstructural alterations and the manner in which substances behave during the heat treatment process.

Finally, studies were conducted on the TE properties of bulk samples obtained from powders processed at different MCS times. As illustrated in (Fig. 6a), the temperature dependence of the electrical conductivity of $Mg_{3.2}Sb_{1.5}Bi_{0.45}Te_{0.05}$ samples with varying MCS times is evident. It is notable that all samples exhibit behaviour consistent with that of heavily doped semiconductors. With increasing temperature, the electrical conductivity, σ, initially increases, reaching a maximum in the range of 550–700 K, and then begins to decrease slightly. The highest electrical conductivity values across the entire temperature range are demonstrated by the sample obtained after 1 hour of MCS, which may be related to the grain size.

The temperature dependencies of the Seebeck coefficient are demonstrated in (Fig. 6b). It is evident that all samples exhibit negative S values, thereby suggesting n-type conductivity. The absolute value of the Seebeck coefficient $|S|$ increases monotonically with temperature for all samples. The sample obtained after 1 hour of MCS has the lowest value of $|S| \approx 205\ \mu V\ K^{-1}$ at 765 K, while the other samples have higher values with $|S| \approx 255\ \mu V\ K^{-1}$ at 765 K. Concurrently, the Seebeck coefficient values of all samples from 3 to 9 hours of grinding are within the same range.

As illustrated in (Fig. 6c), the power factor ($PF = S^2\sigma$) is dependent on temperature. The optimal combination of electrical conductivity and Seebeck coefficient is demonstrated by the sample sintered after 5 hours of MCS, which exhibits the best power factor values. The maximum PF value is approximately 16 μW ($cm^{-1}\ K^{-2}$), which is observed at the temperature around 650 K.

As illustrated in (Fig. 7a), the temperature dependence of the total thermal conductivity, κ, is demonstrated. Within the temperature range of 395 to 580 K, it is evident that the values of κ undergo a decline in proportion to the rise in temperature. It is evident from the data that there is a slow decrease in values for all samples above 580 K. Following a 1-hour MCS, the sample exhibits elevated thermal conductivity, a phenomenon attributable primarily to its comparatively larger grain size in comparison to other samples. The minimum value of $\kappa \approx 1.25\ W$ ($m^{-1}\ K^{-1}$) is demonstrated by the sample after 3 hours of MCS at a temperature of 580 K.

The electronic component of thermal conductivity κ_{el}, calculated according to the Wiedemann–Franz law, is demonstrated in (Fig. 7b). It is evident that, in accordance with the behaviour of electrical conductivity, there is a monotonic increase in κ_{el} with an increase in temperature. The most significant contribution of the electronic component is observed in the sample sintered after 1 hour of MCS, which demonstrates maximum electrical conductivity.

As illustrated in (Fig. 7c), the temperature dependence of the lattice thermal conductivity κ_{lat} is depicted as the difference κ_{lat}
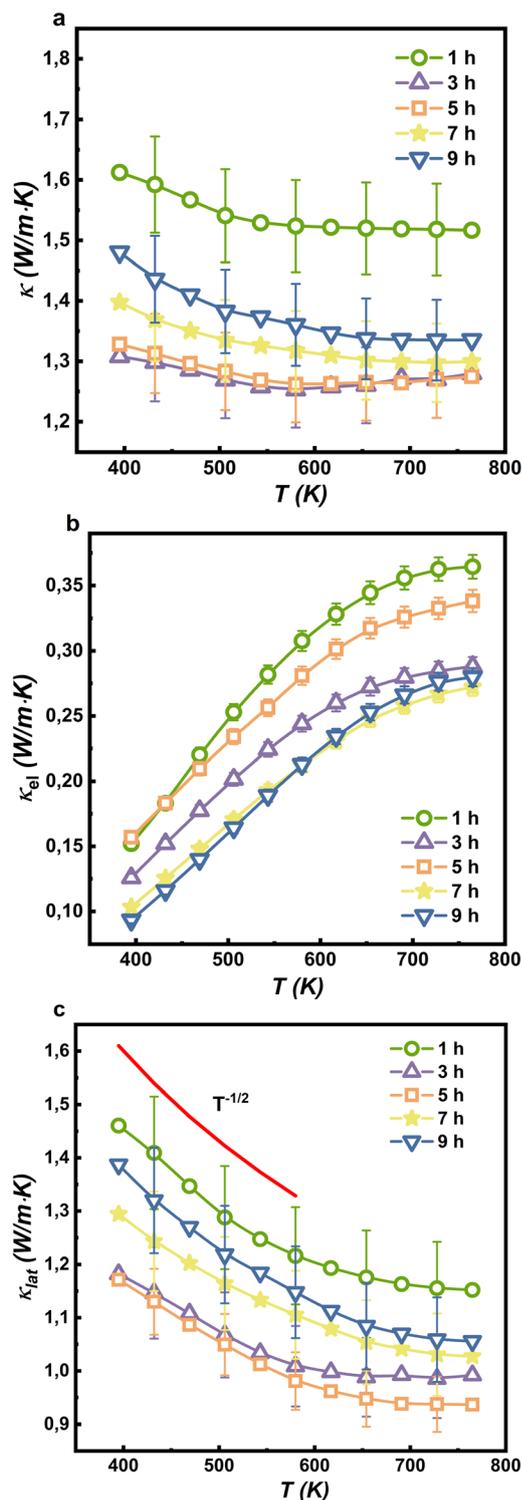
Fig. 7 Temperature dependencies of (a) total, (b) electronic, and (c) lattice thermal conductivities of bulk $Mg_{3.2}Sb_{1.5}Bi_{0.45}Te_{0.05}$ samples obtained by MCS with varying times from 1 to 9 hours and after SPS.

with the Klemens–Callaway model,[33,34] which suggests that the observed scattering is due to point defects. Indeed, such a dependence is characteristic of the compounds under consideration, in which point defects such as vacancies, alloy disorder scattering, interstitial atoms, and impurity atoms are present.[27,35,36] Across the entire temperature range, the lattice contribution values for the sample sintered after 5 hours of MCS demonstrate minimal values. Consequently, this particular sample attains the minimum value of $\kappa_{lat} \approx 0.93$ W $(m^{-1}\,K^{-1})$ at $T = 765$ K, a pivotal factor in attaining a high TE figure of merit.

Fig. 8a presents the temperature dependence of the TE figure of merit of the samples obtained after varying MCS times. For all compositions, the dimensionless parameter zT increases linearly with increasing temperature, reaching a maximum near 765 K. The maximum value of zT is approximately 0.92 at 765 K, demonstrated by the sample sintered after 5 hours of MCS. The elevated figure of merit is indicative of a synergistic optimisation of transport properties. This specimen exhibits a high electrical conductivity, which is commensurate with that of the
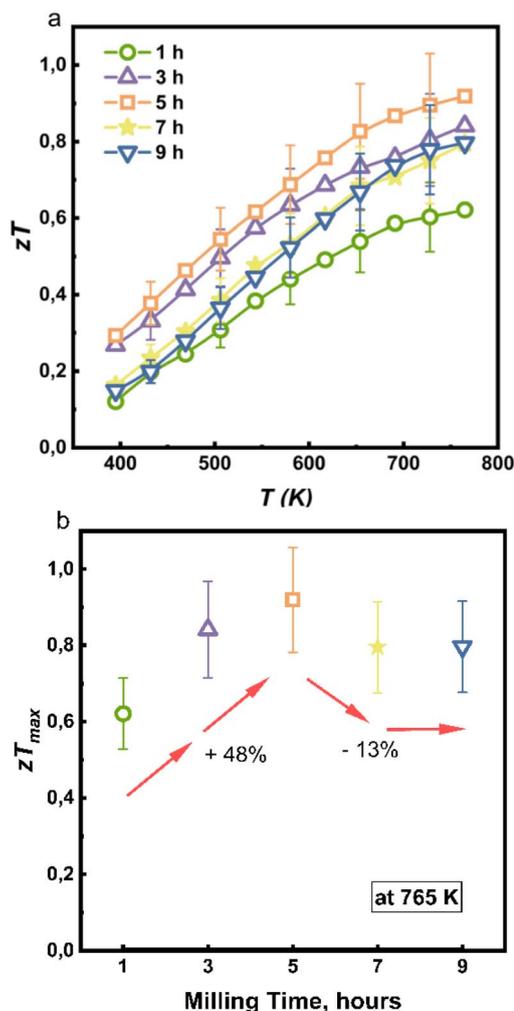

Fig. 8 (a) Temperature dependence of the TE figure of merit and (b) maximum values of the TE figure of merit of bulk $Mg_{3.2}Sb_{1.5}Bi_{0.45}Te_{0.05}$ samples obtained by MCS with varying times from 1 to 9 hours and after SPS.

$= \kappa - \kappa_{el}$. The values obtained for all samples decrease across the entire temperature range and have a dominant contribution to the overall thermal conductivity. Within the temperature range of 395–580 K, the lattice thermal conductivity of all samples is described by the $T^{-1/2}$ dependence. This is consistent

specimen following 1 hour of grinding. This, in turn, results in a high power factor. Simultaneously, it has been demonstrated that a duration of 5 hours of grinding results in a substantial reduction of the total thermal conductivity, achieved by minimising the lattice component. The sample obtained after 1 hour of MCS demonstrates a considerably diminished figure of merit, attributable to the low power factor, particularly the Seebeck coefficient, despite elevated electrical conductivity values.

Fig. 8b demonstrates that with an augmentation in grinding time from 1 to 5 hours, the TE figure of merit of the samples exhibits a 48% increase. An additional augmentation in MCS time from 7 to 9 hours results in a 13% diminution in the figure of merit, culminating in stabilisation at $zT \approx 0.8$ at 765 K.

The proposed approach, which combines morphological and phase analysis, enables significant optimisation of synthesis parameters. This approach has been shown to reduce processing time without compromising the quality of the final product. The stabilisation of particle sizes after 5 hours of grinding indicates the possibility of minimising energy consumption in the production of TE materials of this class.

4   Conclusions

In this study, powders of the thermoelectric material $Mg_{3.2}Sb_{1.5}Bi_{0.45}Te_{0.05}$ were obtained by mechanochemical synthesis with varying times from 1 to 9 hours. Experimentally, it was determined that the optimal MCS time for $Mg_{3.2}Sb_{1.5}Bi_{0.45}Te_{0.05}$ is 5 hours. Within this time frame, the formation of the target α-phase is completed, a median particle size of 3.7 μm is achieved, and the most uniform particle size distribution is observed. The thermoelectric figure of merit of the sample obtained from the powder after 5 hours of MCS is $zT \approx 0.92$ at 765 K. This MCS time is optimal under the existing conditions due to the resulting particle size distribution, which allows the synthesis of a microstructure that determines suitable thermoelectric characteristics. A comprehensive approach combining phase and morphological analysis allows a significant reduction in the synthesis time from 10–20 hours to 5 hours.

Author contributions

A. A. Mikhailova: article concept, literature search, article writing, conducting experiments. A. A. Markin: examination of the samples using a scanning electron microscope, image processing. K. A. Shcherbakova: analysis of the results obtained from SEM and phase analysis. Yu. M. Kuznetsov: measurement of thermoelectric properties and interpretation of the results. V. A. Dybov: forming the direction of research and tasks to be solved, critical review of the content, concept design, approval of the final version of the article. N. Yu. Tabachkova: assistance in conducting experiments.

Conflicts of interest

The authors declare that there are no conflicts of interest to disclose in this article.

Data availability

Datasets for this article, including a series of SEM images of powders after different times of mechanochemical synthesis, a series of SEM images of powders after different times of mechanochemical synthesis after image processing and histograms of the distribution of powder particles depending on the time of mechanochemical synthesis, are available at Zenodo at https://doi.org/10.5281/zenodo.18773636.

References

1 G. Snyder and E. Toberer, *Nat. Mater.*, 2008, 7, 105–114, DOI: 10.1038/nmat2090.
2 *Thermoelectrics and its Energy Harvesting*, ed. D. M. Rowe, CRC Press, Boca Raton, 2nd edn, 2018.
3 A. F. Ioffe, *Semiconductor Thermoelements and Thermoelectric Cooling*, Infosearch, 1957.
4 *Novel Thermoelectric Materials and Device Design Concepts*, ed. S. Skipidarov and M. Nikitin, Springer International Publishing, New York, 1st edn, 2019.
5 J. W. Li, Z. Han, J. Yu, H. L. Zhuang, H. Hu, B. Su, H. Li, Y. Jiang, L. Chen, W. Liu, Q. Zheng and J. F. Li, *Nat. Commun.*, 2023, 14, 7428, DOI: 10.1038/s41467-023-43228-9.
6 Q. Zhu, S. Song, H. Zhu and Z. Ren, *J. Power Sources*, 2019, 414, 343–400, DOI: 10.1016/j.jpowsour.2019.01.022.
7 Z. Liu, N. Sato, W. Gao, K. Yubuta, N. Kawamoto, M. Mitome, K. Kurashima, Y. Owada, K. Nagase, C.-H. Lee, J. Yi, K. Tsuchiya and T. Mori, *Joule*, 2021, 5, 1196–1208, DOI: 10.1016/j.joule.2021.03.017.
8 J. Zhang, L. Song, S. H. Pedersen, H. Yin, L. T. Hung and B. B. Iversen, *Nat. Commun.*, 2017, 8, 13901, DOI: 10.1038/ncomms13901.
9 E. Zintl and E. Z. Husemann, *Phys. Chem.*, 1933, B21, 138–155, DOI: 10.1515/zpch-1933-2112.
10 A. Bhardwaj, A. Rajput, A. K. Shukla, J. J. Pulikkotil, A. K. Srivastava, A. Dhar, G. Gupta, S. Auluck, D. K. Misra and R. C. Budhani, *RSC Adv.*, 2013, 3, 8504–8516, DOI: 10.1039/C3RA40457A.
11 H. Shang, Z. Liang, C. Xu, J. Mao, H. Gu, F. Ding and Z. Ren, *Research*, 2020, 2020, 1219461, DOI: 10.34133/2020/1219461.
12 S. H. Kim, C. M. Kim, Y. K. Hong, K. O. Sim, J. H. Kim, T. Onimaru, T. Takabatake and M. H. Jung, *Mater. Res. Express*, 2015, 2, 055903, DOI: 10.1088/2053-1591/2/5/055903.
13 J. Zhang, L. Song and B. B. Iversen, *Comput. Mater. Sci.*, 2019, 5, 76, DOI: 10.1038/s41524-019-0215-y.
14 X. Y. Chong, P. W. Guan, Y. Wang, S. L. Shang, J. P. Soldan Palma, F. Drymiotis, A. R. Vilupanur, K. E. Star, J. P. Fleurial and Z. K. Liu, *ACS Appl. Energy Mater.*, 2018, 1, 11, DOI: 10.1021/acsaem.8b01520.
15 Y. Wang, X. Zhang, Y. Wang, H. Liu and J. Zhang, *Phys. Status Solidi A*, 2019, 216, 1800811, DOI: 10.1002/pssa.201800811.
16 S. Ohno, K. Imasato, S. Anand, H. Tamaki, S. D. Kang, P. Gorai, H. K. Sato, E. S. Toberer, T. Kanno and G. J. Snyder, *Joule*, 2018, 2, 141–154, DOI: 10.1016/j.joule.2017.11.005.

17 J. Mao, Y. Wu, S. Song, Q. Zhu, J. Shuai, Z. Liu, Y. Pei and Z. Ren, *ACS Energy Lett.*, 2017, **2**, 2245–2250, DOI: 10.1021/acsenergylett.7b00742.

18 J. Xin, G. Li, G. Auffermann, H. Borrmann, W. Schnelle, J. Gooth, X. Zhao, T. Zhu, C. Felser and C. Fu, *Mater. Today Phys.*, 2018, **7**, 61–68, DOI: 10.48550/arXiv.2003.13313.

19 S. W. Song, J. Mao, M. Bordelon, R. He, Y. M. Wang, J. Shuai, J. Y. Sun, X. B. Lei, Z. S. Ren, S. Chen, S. Wilson, K. Nielsch, Q. Y. Zhang and Z. F. Ren, *Mater. Today Phys.*, 2019, **8**, 25–33, DOI: 10.1016/j.mtphys.2018.12.004.

20 J. Shuai, Y. Wang, H. S. Kim, Z. Liu, J. Sun, S. Chen, J. Sui and Z. Rena, *Acta Mater.*, 2015, **93**, 187–193, DOI: 10.1016/j.actamat.2015.04.023.

21 Y. Wang, X. Zhang, Y. Liu, Y. Wang, H. Liu and J. Zhang, *J. Materiomics*, 2020, **6**, 216–223, DOI: 10.1016/j.jmat.2019.12.007.

22 W. Zhu, P. Zheng, Y. Shao, W. Fang, H. Wu and J. Si, *J. Alloys Compd.*, 2022, **924**, 166598, DOI: 10.1016/j.jallcom.2022.166598.

23 C. Xu, Z. Liang, H. Shang, D. Wang, H. Wang, F. Ding, J. Mao and Z. Ren, *Mater. Today Phys.*, 2021, **17**, 100336, DOI: 10.1016/j.mtphys.2020.100336.

24 K. Kihou, H. Kunioka, H. Nishiate and C. H. Lee, *J. Mater. Res. Technol.*, 2021, **10**, 438–444, DOI: 10.1016/j.jmrt.2020.12.008.

25 L. Hu, Q. Zhang, Z. Shan, L. Wang, Y. Zheng and J. Fan, *Scr. Mater.*, 2023, **235**, 115629, DOI: 10.1016/j.scriptamat.2023.115629.

26 Z. Liu, W. Gao, H. Oshima, K. Nagase, C.-H. Lee and T. Mori, *Nat. Commun.*, 2020, **13**, 1120, DOI: 10.1038/s41467-022-28798-4.

27 L. Wang, W. Zhang, S. Y. Back, N. Kawamoto, D. H. Nguyen and T. Mori, *Nat. Commun.*, 2024, **15**, 6800, DOI: 10.1038/s41467-024-51120-3.

28 J. Tani and H. Ishikawa, *Mater. Lett.*, 2020, **262**, 127056, DOI: 10.1016/j.matlet.2019.127056.

29 J. Li, S. Zhang, F. Jia, S. Zheng, X. Shi, D. Jiang, S. Wang, G. Lu, L. Wu and Z.-G. Chen, *Mater. Today Phys.*, 2020, **15**, 100269, DOI: 10.1016/j.mtphys.2020.100269.

30 X. Yang, H. Ni, X. Yu, B. Cao, J. Xing, Q. Chen, L. Xi, J. Liu, J. Zhang, K. Guo and J.-T. Zhao, *J. Materiomics*, 2024, **10**, 154–162, DOI: 10.1016/j.jmat.2023.05.004.

31 N. Otsu, *IEEE Trans. Syst. Man Cybern.*, 1979, **9**, 62, DOI: 10.1109/TSMC.1979.4310076.

32 P. Pfaff, *Forsch. Ingenieurwes.*, 1940, **11**, 188–202, DOI: 10.1007/BF02593972.

33 P. G. Klemens, *Phys. Rev.*, 1960, **119**(2), 507–509, DOI: 10.1103/PhysRev.119.507.

34 J. Callaway, *Phys. Rev.*, 1960, **120**(4), 1149–1154, DOI: 10.1103/PhysRev.120.1149.

35 T. Kanno, H. Tamaki, M. Yoshiya, H. Uchiyama, S. Maki, M. Takata and Y. Miyazaki, *Adv. Funct. Mater.*, 2021, **31**(13), 2008469, DOI: 10.1002/adfm.202008469.

36 J. Jia, Y. Zhou, X. Chen, W. Xue, H. Yu, J. Li, S. Zhi, C. Chen, J. Wang, S. Hou, X. Liu, Y. Wang, F. Cao, Y. Chen, J. Mao and Q. Zhang, *Research*, 2022, **2022**, 9875329, DOI: 10.34133/2022/9875329.